^{6}Li global phenomenological optical model potential

Yongli Xu,[1,*] Yinlu Han,[2,†] Jiaqi Hu,[2] Haiying Liang,[2] Zhendong Wu,[2] Hairui Guo,[3] and Chonghai Cai[4]

[1]*College of Physics and Electronic Science, Shanxi Datong University, Datong 037009, China*

[2]*Key Laboratory of Nuclear Data, China Institute of Atomic Energy, P.O. Box (275-41), Beijing 102413, China*

[3]*Institute of Applied Physics and Computational Mathematics, Beijing 100094, China*

[4]*Department of Physics, Nankai University, Tianjin 300071, China*

(Received 5 June 2018; published 22 August 2018)

A systematic global phenomenological optical model potential for a ^{6}Li projectile is established by studying the experimental data of elastic-scattering angular distributions and reaction cross sections from ^{24}Mg to ^{209}Bi below 250 MeV. Based on the obtained ^{6}Li global phenomenological optical model potential, the extensive analysis of ^{6}Li elastic scattering is performed for different targets by comparing with the corresponding experimental data. It is found that the results calculated using the global optical model potential are consistent with a large body of elastic-scattering data for the reactions involving ^{6}Li incidence. Application of the global potential is performed to predict the elastic-scattering angular distributions and reaction cross sections for those targets outside of the mass range. The reasonable results are also obtained.

DOI: 10.1103/PhysRevC.98.024619

I. INTRODUCTION

The optical model is one of the most fundamental theoretical models in nuclear reaction theory [1]. The optical model potential (OMP) is the key to the model. It is commonly used in nuclear reaction theory as effective interactions that take into account the complexity of the many-body effects in nucleon-nucleus scattering. In particular, the global phenomenological OMP is of interest to determine because it can be used to reliably predict basic observables in some energies and nuclides regions where no experimental measurement data exist [2].

The study of nuclear reactions involving weakly bound projectiles has been a subject of extensive experimental and theoretical studies in recent years. The reason is the observation of several unusual features compared to the case of strongly bound projectiles since the projectiles are weakly bound nuclei, characterized by low-breakup threshold, cluster structure, and diffuse matter distribution. Thus, the breakup and transfer mechanisms are of crucial importance in these reactions [3]. By studying these reactions, it is possible to investigate the role played by breakup and transfer mechanisms on the reaction process.

Especially for the ^{6}Li projectile it has always been of interest for both experimental and theoretical nuclear physicists. Since it breaks up into $\alpha + d$ and has low threshold breakup energies of 1.47 MeV, the breakup effect has been studied on the basis of different methods [4,5]. In addition, unexpected energy dependence of the optical model parameters around the Coulomb barrier, namely, a threshold anomaly, have been also widely studied for the ^{6}Li projectile [3,6]. On the other hand, the ^{6}Li projectile is also the object of many studies aiming to build a bridge between the elastic scattering of light and heavy ions because it is the lightest heavy-ion projectile [7,8]. In these studies, the phenomenological OMP for the ^{6}Li projectile has been widely used to analyze heavy-ion scattering data in terms of empirical Woods-Saxon parametrizations of the nuclear potential. Furthermore, all reactions involving ^{6}Li in entrance or exit channels again require the ^{6}Li OMP as input. However, the potential for one nucleus at a particular energy may reflect the peculiarities of that nucleus and may not be suitable for neighboring nuclei at different energies. Therefore, it is essential to investigate a set of reliable global optical model parameters for use in the reaction involving ^{6}Li incidence or emission. Besides the obvious utilitarian value of such parameters, there is also a reason to believe that useful information about nuclear forces and nuclear structure can be obtained from the systematic analysis of ^{6}Li elastic scattering by the global OMP.

So far, there have been only few preliminary reports on the investigation of the global phenomenological OMP parameters for ^{6}Li. Most of them are for individual target and single incident energies. In earlier research, a set of global phenomenological OMP parameters of ^{6}Li [9] was obtained for 44 sets of ^{6}Li data covering the mass range of 24–208 and an energy range of 13–156 MeV. However, the considered less and old elastic-scattering angular distribution measurement as well as the neglected reaction cross sections in the fitting may lead to a large uncertainty of the parameters. On the other hand, there has been a large amount of new experimental data over a wider range of energies and angles for ^{6}Li scattering from different targets so far. It is enough to investigate on a set of new ^{6}Li global phenomenological OMPs by constructing mass number and energy dependence of the optical model parameters.

In light of the above considerations, in this paper, we aim to establish a global phenomenological OMP of the Woods-Saxon type for the ^{6}Li projectile by fitting the experimental

*xuyongli776@126.com

†hanyl@ciae.ac.cn

TABLE I. The $d\sigma/d\Omega$ database for the ^{6}Li elastic scattering. E is the incident energy for different targets in the laboratory system.

Target	E (MeV)	Reference
^{24}Mg	240.0	[12]
^{25,26}Mg	34.0	[13]
^{27}Al	7.0,8.0,10.0,12.0,18.0	[14]
	34.0	[13]
^{28}Si	7.5,9.0,11.0,13.0	[3]
	16.0,21.0	[15]
	13.0,20.0,25.0	[16]
	27.0,34.0	[17]
	46.0	[9]
	99.0	[18]
	135.0	[19]
	154.0	[20]
	210.0	[21]
	240.0	[12]
^{39}K	34.0	[22]
^{40}Ca	50.6	[23]
	99.0	[18]
	156.0	[24]
	210.0	[21]
	240.0	[25]
^{48}Ca	240.0	[25]
^{54}Fe	38.0,44.0,50.0	[26]
^{59}Co	12.0,18.0,26.0,30.0	[27]
^{58}Ni	9.85,11.21,12.13,13.04,14.04	[28]
	34.0	[29]
	50.6	[23]
	73.7	[30]
	90.0	[31]
	99.0	[18]
	210.0	[32]
	240.0	[33]
^{65}Cu	25.0	[34]
^{64}Zn	12.0,13.0,13.8,15.0,16.5,18.0,20.0,22.0	[35]
^{80}Se	14.0,14.5,15.0,15.5,16.0,17.0,18.0,19.0,20.0,22.19, 23.0,26.0	[36]
^{89}Y	60.0	[37]
^{90}Zr	11.0,12.0,13.0,15.0,17.0,19.0,21.0,25.0,30.0	[38]
	34.0	[39]
	60.0	[37]
	70.0	[40]
	73.7	[30]
	99.0	[18]
	156.0	[9]
	210.0	[21]
	240.0	[33]
^{91}Zr	34.0	[39]
^{112}Sn	21.0,23.0,25.0,35.0	[41]
	22.0,30.0	[42]
^{116}Sn	20.0,21.0,22.0,23.0,24.0,26.0,30.0,35.0,40.0	[43]
^{118}Sn	42.0	[44]
^{120}Sn	30.0	[45]
	44.0	[46]
	90.0	[31]
^{124}Sn	73.7	[30]
^{138}Ba	21.0,22.0,23.0,24.0,26.0,28.0	[47]
^{144}Sm	21.0,22.1,22.6,24.1,26.0,28.0,30.1,32.2,35.1,42.3	[48]
^{208}Pb	25.0,29.0,31.0,33.0,35.0,37.0,43.0,46.0	[49]
	29.0,33.0,39.0	[50]
	36.0,42.0,48.0	[51]
	50.6	[23]
	73.7	[30]
	88.0	[52]
	90.0	[31]
	99.0	[18]
	156.0	[9]
	210.0	[21]
^{209}Bi	24.0,26.0,28.0,30.0,32.0,34.0,36.0,38.0,40.0, 44.0,50.0	[53]
	29.9,32.8	[54]
	36.0,40.0	[55]

data of the elastic-scattering angular distributions and reaction cross sections from ^{24}Mg to ^{209}Bi targets with incident energies below 250 MeV. Furthermore, the elastic-scattering angular distributions and reaction cross sections are predicted for those targets outside of the mass range.

This paper is organized as follows. In Sec. II, we outline the formalism of the calculation and describe the method in detail. We also give the selected experimental data and present a new set of ^{6}Li global OMP parameters. In Sec. III, we display the comparisons of calculated results with experimental data. Finally, a brief summary and our conclusions are contained in Sec. IV.

II. THE GLOBAL PHENOMENOLOGICAL OPTICAL MODEL POTENTIAL AND PARAMETERS

A. Form of the optical model potential

The optical potential used in the analysis of the data is of conventional form, containing a complex nuclear central term and a Coulomb term,

$$V(r, E) = V_R(r, E) + i[W_S(r, E) + W_V(r, E)] + V_C(r), \quad (1)$$

where V_R represents the real part potential and W_S and W_V are the surface and volume absorption imaginary part potentials, respectively. $V_C(r)$ is the Coulomb potential. No spin-orbit potential term is included since the relatively weak spin-orbit interaction for ^{6}Li has little influence on the differential cross section.

The most widely used shape for the potentials of real and imaginary parts is the Woods-Saxon form factors. The real part of the OMP, the imaginary parts for volume absorption and surface absorption of the OMP, respectively, are expressed as

$$V_R(r, E) = -\frac{V_R(E)}{1 + \exp[(r - R_R)/a_R]}, \quad (2)$$

$$W_V(r, E) = -\frac{W_V(E)}{1 + \exp[(r - R_V)/a_V]}, \quad (3)$$

$$W_S(r, E) = -4W_S(E)\frac{\exp[(r - R_S)/a_S]}{\{1 + \exp[(r - R_S)/a_S]\}^2}. \quad (4)$$

TABLE II. The reaction cross-sectional database for the ^{6}Li projectile.

Target	Reference
^{27}Al	[56,57]
$^{nat.}$Li	[58]
^{64}Zn	[35,59]
^{112,116}Sn	[41]
^{138}Ba	[47]
^{208}Pb	[50,60]

The Coulomb potential V_C is taken to be that of a uniformly charged sphere with a charge equal to Z of the target nucleus and a radius equal to R_C. Thus it has the form

$$V_C(r) = \begin{cases} \frac{zZe^2}{2R_C}\left(3 - \frac{r^2}{R_C^2}\right), & r < R_C, \\ \frac{zZe^2}{r}, & r \geqslant R_C, \end{cases} \tag{5}$$

where z is the charge of the ^{6}Li projectile.

The potential depth is dependent on incident energies (E in MeV) and given by

$$V_R(E) = V_0 + V_1 E, \tag{6}$$

$$W_S(E) = \max\{0, W_0 + W_1 E\}, \tag{7}$$

$$W_V(E) = \max\{0, U_0 + U_1 E + U_2 E^2\}. \tag{8}$$

The radii of these potentials are dependent on target masses (A),

$$R_i = r_i A^{1/3}, \quad i = R, S, V, C, \tag{9}$$

where r_R, r_S, r_V, and r_C are the radius parameters of the real part, the imaginary part of the surface absorption, the imaginary part of the volume absorption, and the Coulomb potential, respectively. The a_R, a_S, and a_V mentioned in Eqs. (2)–(4) are the corresponding diffuseness widths. The parameters V_0, V_1, W_0, W_1, U_0, U_1, U_2, r_R, r_S, r_V, r_C, a_R, a_S, and a_V can be adjusted.

B. Parametrization of the optical model potential

We have made an effort to collect nearly all the experimental data of elastic-scattering angular distributions and reaction cross sections for the ^{6}Li projectile that could be found in the electronically available literature. They include those targets for the mass of $24 \leqslant A \leqslant 209$ with incident energies below 250 MeV. The complete references for these experimental databases of the elastic-scattering angular distributions and reaction cross sections for the ^{6}Li projectile are listed in Tables I and II.

The adjustment of the optical potential parameters is performed automatically with a computer code to minimize a quantity called χ^2, which represents the deviation of the calculated results from experimental values. We first get χ^2 for each single target and then obtain the average value of total χ^2 for all targets. χ_i^2 for each target at all energy points, here i and j, respectively, indicating each target nucleus and each energy point, is defined as follows:

TABLE III. The global phenomenological OMP parameters for ^{6}Li.

Parameter	Value	Unit
V_0	265.736	MeV
V_1	−0.183	
W_0	28.850	MeV
W_1	−0.0989	
U_0	−5.226	MeV
U_1	0.118	
U_2	0.000379	
r_R	1.120	fm
r_S	1.311	fm
r_V	1.537	fm
r_C	1.674	fm
a_R	0.814	fm
a_S	0.939	fm
a_V	0.726	fm

$$\chi^2_{i,\mathrm{el}} = \frac{1}{N_{i,\mathrm{el}}} \sum_{j=1}^{N_{i,\mathrm{el}}} \frac{1}{K_{i,j,\mathrm{el}}} \sum_{k=1}^{K_{i,j,\mathrm{el}}} \left[\frac{\sigma^T_{i,j,\mathrm{el}}(\theta_{i,j,k}) - \sigma^E_{i,j,\mathrm{el}}(\theta_{i,j,k})}{\Delta\sigma^E_{i,j,\mathrm{el}}(\theta_{i,j,k})} \right]^2, \tag{10}$$

$$\chi^2_{i,\mathrm{re}} = \frac{1}{N_{i,\mathrm{re}}} \sum_{j=1}^{N_{i,\mathrm{re}}} \left[\frac{\sigma^T_{i,\mathrm{re}}(j) - \sigma^E_{i,\mathrm{re}}(j)}{\Delta\sigma^E_{i,\mathrm{re}}(j)} \right]^2. \tag{11}$$

The average value of the total χ^2 is

$$\chi^2 = \frac{1}{N} \sum_{i=1}^{N} \frac{W_{i,\mathrm{el}}\chi^2_{i,\mathrm{el}} + W_{i,\mathrm{re}}\chi^2_{i,\mathrm{re}}}{W_{i,\mathrm{el}} + W_{i,\mathrm{re}}}, \tag{12}$$

where $N_{i,\mathrm{el}}$ and $N_{i,\mathrm{re}}$ are energy point numbers of the experimental elastic-scattering angular distributions and reaction cross sections for the ith nucleus. $K_{i,j,\mathrm{el}}$ is the angle numbers of the experimental elastic-scattering angular distributions. The superscripts T and E represent the theoretical and experimental values, respectively. $\sigma_{i,j,\mathrm{el}}(\theta_{i,j,k})$ and $\sigma_{i,\mathrm{re}}(j)$ are the elastic-scattering angular distributions for the kth outgoing angle and reaction cross sections, and $\Delta\sigma$ is the experimental error of corresponding data. $W_{i,\mathrm{el}}$ and $W_{i,\mathrm{re}}$ are the weight of the experimental elastic-scattering angular distributions and reaction cross sections for the ith nucleus. At the beginning of optimizing, the weight of them are taken as 1. N is the number of the considered nuclei.

The code APMN [10], which automatically searches optimal optical potential parameters at incident energies below 300 MeV by the improved fastest falling method [11], is further improved and used in the present paper. All the potential parameters' reasonable boundaries of the varied region are given by some physical limitation before the global phenomenological OMP parameters are automatically searched.

On the basis of the elastic-scattering angular distributions and reaction cross sections in the target mass range of $24 \leqslant A \leqslant 209$ below 250 MeV as well as using the improved optimization procedure, the global phenomenological OMP

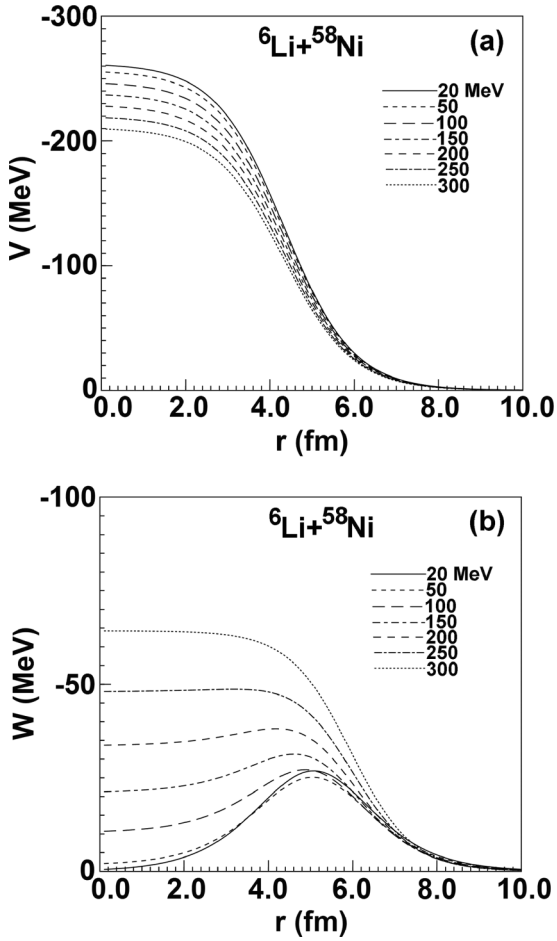

FIG. 1. The radial dependence of our global OMP at incident energies of 20, 50, 100, 150, 200, 250, and 300 MeV for ^{58}Ni. (a) The real part and (b) the imaginary part.

parameters for the ^{6}Li projectile are obtained and presented in Table III.

III. CALCULATED RESULTS AND ANALYSIS

First, the global OMP analysis is performed for the ^{6}Li projectile in this section. Then, the elastic-scattering angular distributions and reaction cross sections are separately calculated using the obtained global phenomenological OMP for ^{6}Li in the target mass range of $24 \leqslant A \leqslant 209$ below 250 MeV. These results are further compared with the corresponding experimental data. For the sake of prediction performance, the elastic-scattering angular distributions and reaction cross sections are also predicted for those targets outside of the mass and energies ranges.

Using the obtained optimum parameters, the radial dependence on the real part and imaginary part of the global OMP are calculated for different targets at incident energies of 20, 50, 100, 150, 200, 250, and 300 MeV, respectively. The results for ^{58}Ni are plotted in Fig. 1. For the real potential, it is observed that the depth linearly decreases with increasing incident energy, and the depth decreases with increasing radius. For the imaginary part potential, the absolute value first

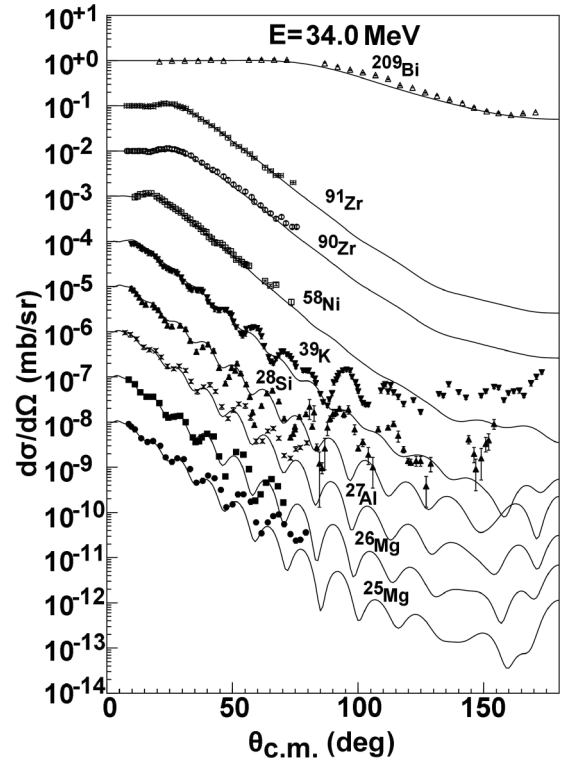

FIG. 2. Calculated elastic-scattering angular distributions in the Rutherford ratio compared with the experimental data [13,17,22,29,39,53] at incident ^{6}Li energies of 34.0 MeV.

increases and then decreases with increasing incident radius. The contribution to the imaginary part of the global OMP changes from the dominant surface absorption into the volume absorption with increasing incident energy, and it is almost from the volume absorption when the incident energy reaches 250 MeV.

Now, we provide a detailed discussion on the elastic-scattering angular distributions calculated using the ^{6}Li global OMP at the same incident energies for different targets by comparing with the existing experiment data.

Figure 2 presents the calculations of elastic-scattering angular distributions in the Rutherford ratio at incident energies of 34.0 MeV for ^{25,26}Mg, ^{27}Al, ^{28}Si, ^{39}K, ^{58}Ni, ^{90,91}Zr, and ^{209}Bi targets. The results are also compared with the experimental data [13,17,22,29,39,53]. One can see that the calculations reproduce the elastic-scattering angular distributions data well except for ^{28}Si and ^{39}K above 90° where the calculations poorly matched in phase with the experimental data. The discrepancy shows that it possibly needs the addition of coupled-channel effects in the backward-angle area for some lighter targets [17,22]. This also indicates the need for a local optical potential to describe the elastic scattering for them in future work.

The comparisons between the calculations of elastic-scattering angular distributions and the experimental data are performed at incident ^{6}Li energies from 42.0 to 46.0 MeV for ^{28}Si, ^{54}Fe, ^{118}Sn, ^{142}Nd, ^{144}Sm, and ^{208}Pb. It is found that the theoretical values are in good agreement with the experimental data [9,26,44,51] for them. Furthermore, the

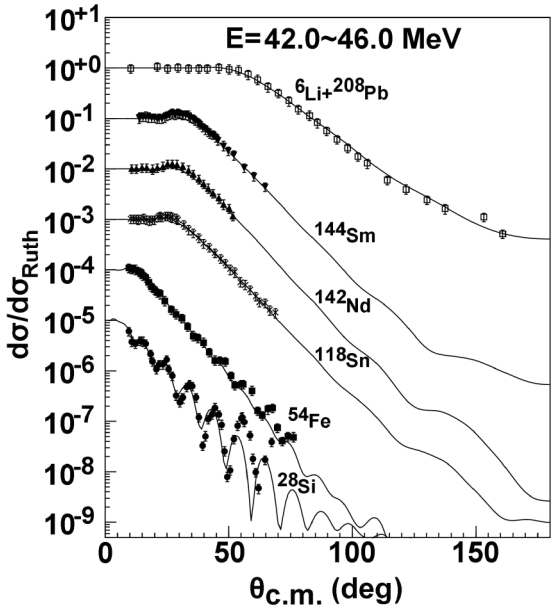

FIG. 3. The same as Fig. 2 but for 42.0–46.0 MeV [9,26,44,51].

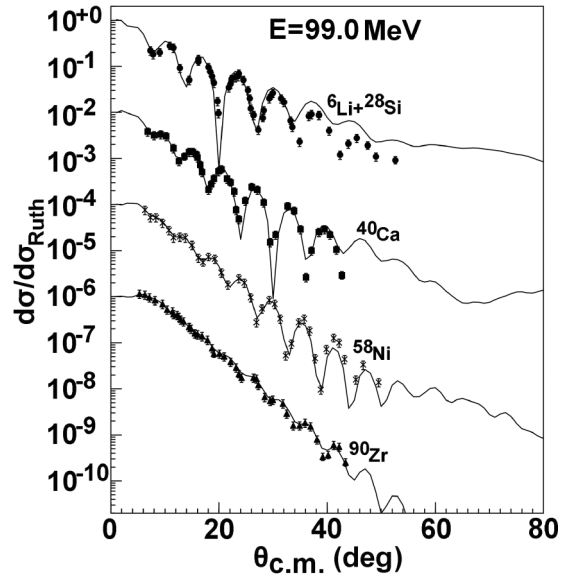

FIG. 5. The same as Fig. 2 but for 99.0 MeV [18].

calculations at incident energies of 50.0 and 50.6 MeV are also compared with the data [23,26] for ^{40}Ca, ^{54}Fe, ^{58}Ni, and ^{208}Pb. Good agreement is also found between our calculations and the measurements. The comparisons for incident energies from 42.0 to 46.0 MeV are given in Fig. 3.

The elastic-scattering angular distributions are calculated and compared with the experimental data [30] at 73.7 MeV for ^{58}Ni, ^{90}Zr, ^{124}Sn, and ^{208}Pb. The results are shown in Fig. 4. It is observed that the calculations can produce good agreement with the experimental results for ^{58}Ni and ^{90}Zr. However, there is a slight overestimation for ^{124}Sn and ^{208}Pb above 50°. For ^{124}Sn, the disagreement should be further verified by the other experimental data. For ^{208}Pb, the detailed discussions can be found in the section for the same target. The elastic-scattering angular distributions at incident energies of 99.0 MeV are also calculated for ^{28}Si, ^{40}Ca, ^{58}Ni, and ^{90}Zr. The comparisons with the experimental data [18] are plotted in Fig. 5. It is clearly shown that there is good agreement between them.

The elastic angular distributions at incident energies of 135.0 and 154.0 MeV are calculated for ^{28}Si. By comparing with the experimental data, it is found that the results are in agreement with the data [19,20], which are shown in Fig. 6. In this figure, the elastic angular distributions at incident energies of 156.0 MeV are also compared with some data for ^{40}Ca and ^{90}Zr. A better description of the experimental data [9,24] is still obtained.

In addition, the elastic-scattering angular distributions at incident ^{6}Li energies of 210.0 MeV are calculated for different targets as is shown in Fig. 7. The calculations are compared

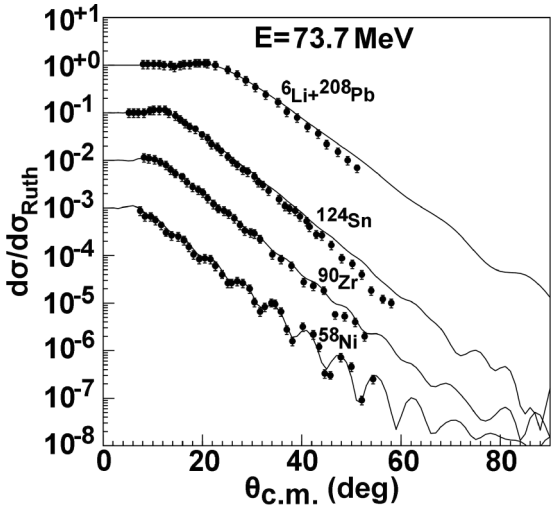

FIG. 4. The same as Fig. 2 but for 73.7 MeV [30].

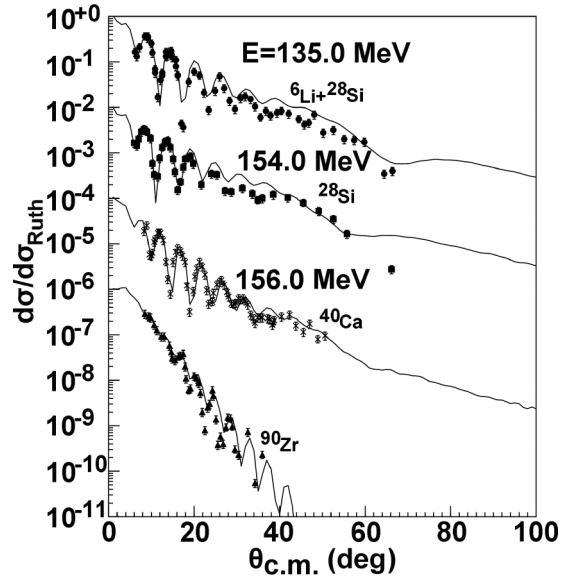

FIG. 6. The same as Fig. 2 but for 135.0–156.0 MeV [9,19,20,24].

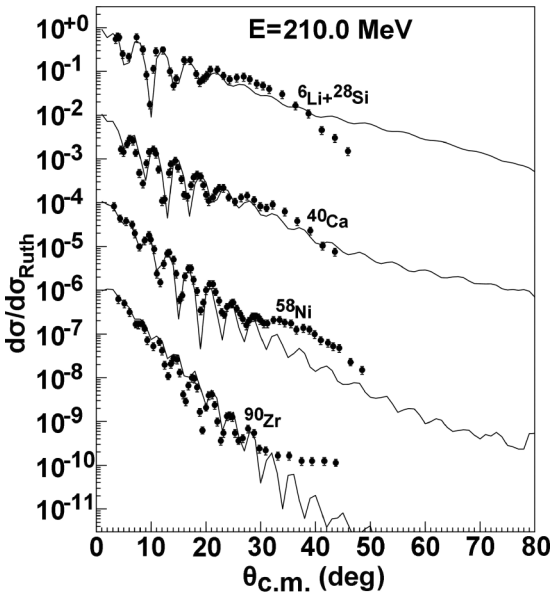

FIG. 7. The same as Fig. 2 but for 210.0 MeV [21,32].

with some data from the same experiment [21,32]. From these comparisons, one can see that good agreement is given for ^{28}Si and ^{40}Ca. But an important discrepancy between the calculations and the data occurs above 30° for ^{58}Ni and ^{90}Zr. The elastic angular distributions at 240.0 MeV are also compared with the experimental data [12,25,33]. These data are also from the same experiment. These results are shown

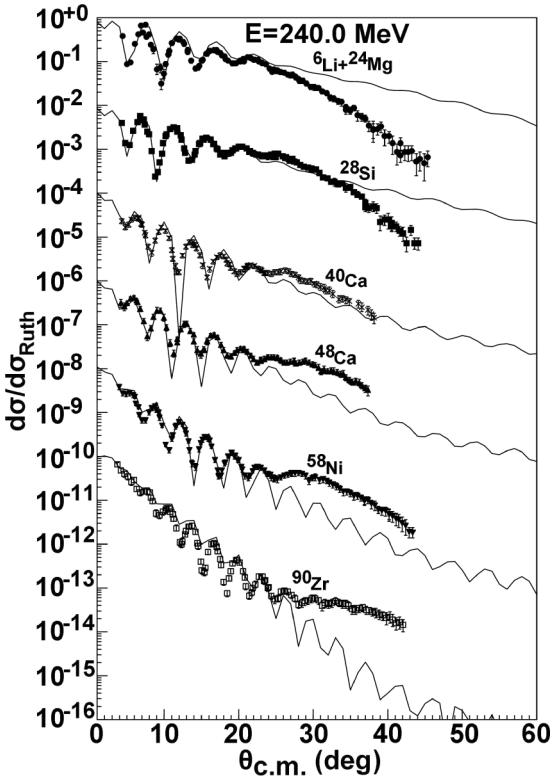

FIG. 8. The same as Fig. 2 but for 240.0 MeV [12,25,33].

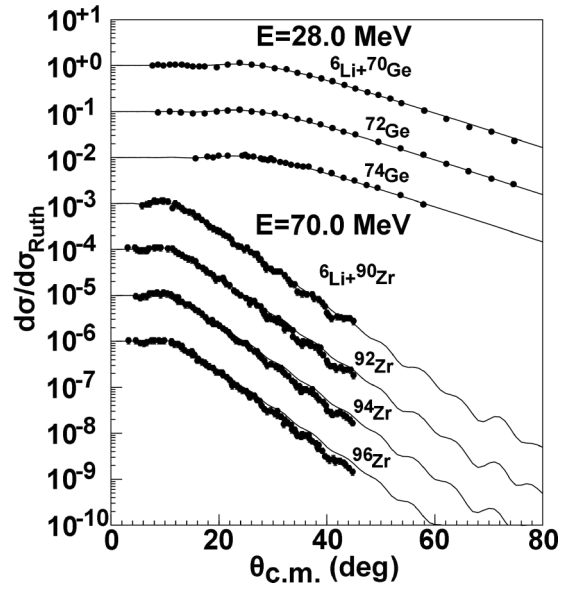

FIG. 9. The same as Fig. 2 but for 28.0 and 70.0 MeV [40,65].

in Fig. 8. One can see that there are some divergence between the calculations and the experimental data above 25° for some targets. The reason may be from the neglect coupling effect between the elastic channel and the other reaction mechanisms at higher incident energies. Such issues require performing a coupled-channel calculation using the coupled discretized continuum channel (CDCC) method, which considers the breakup effects of the projectile ^{6}Li [33,61–64].

To test the reliability of global OMP for the isotope with the target mass number increasing, the elastic-scattering angular distributions for the isotope chains of some targets are

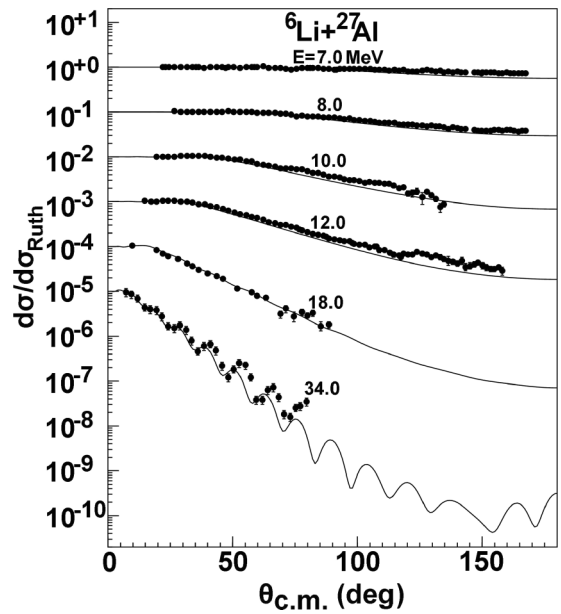

FIG. 10. Calculated elastic-scattering angular distributions in the Rutherford ratio compared with the experimental data [13,14] for ^{27}Al.

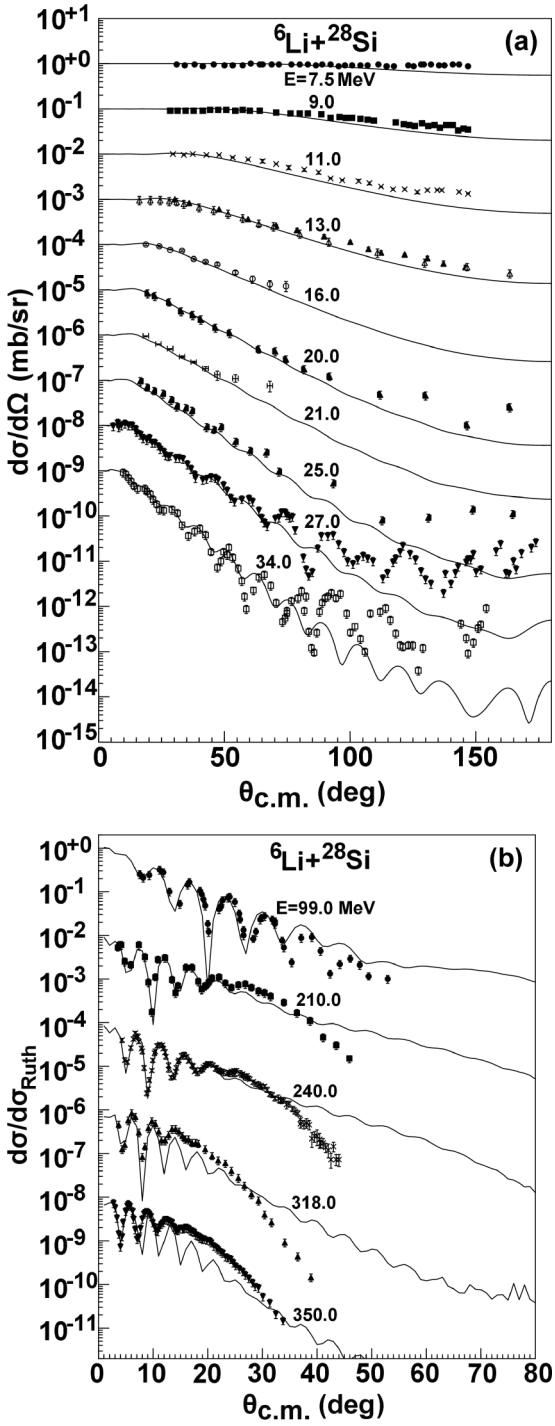

FIG. 11. The same as Fig. 10 but for ^{28}Si [3,12,15–18,21,66,67].

predicted and compared with the existing experimental data at the same incident energies. These data are from the same experiment. Figure 9 gives the comparisons of elastic-scattering angular distributions with the corresponding experimental data [40,65] for isotope chain ^{70,72,74}Ge at 28.0 MeV together with that of ^{90,92,94,96}Zr at 70.0 MeV. As can be seen from the figure, good agreement is obtained between the theoretical results and the experimental data.

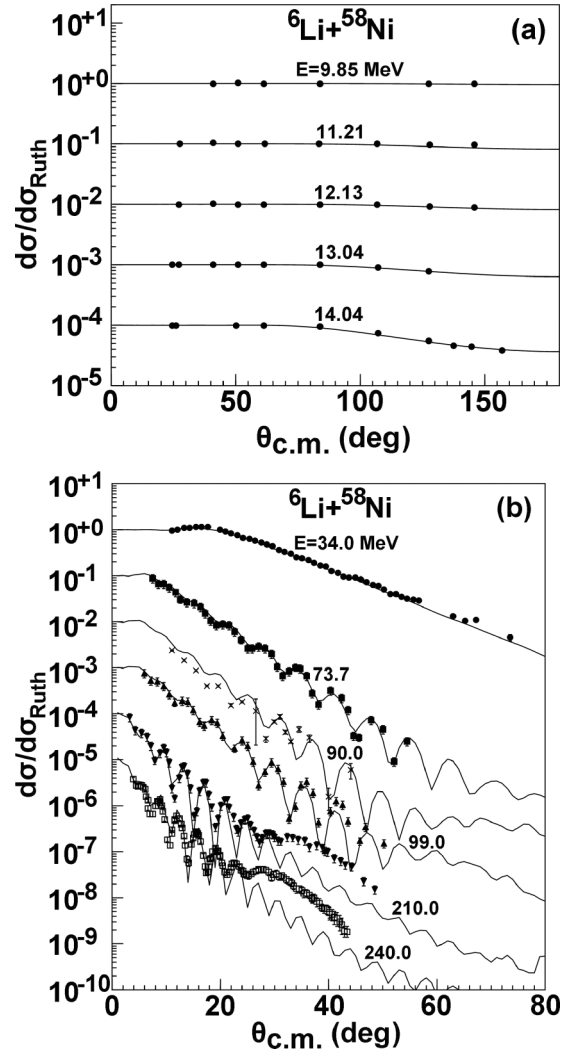

FIG. 12. The same as Fig. 10 but for ^{58}Ni [18,23,25,28–32].

Next, the elastic-scattering angular distributions for the same target at different incident energies are calculated using the obtained ^{6}Li global OMP. Figure 10 displays the comparisons with the experimental data [13,14] for ^{27}Al. A good fit is found between them below 34.0 MeV.

For ^{28}Si, the calculations of elastic-scattering angular distributions are also compared with the experimental data [3,12,15–18,21] at incident energies from 7.5 to 240 MeV, which is shown in Fig. 11. It is observed that the calculations agree with the experimental data below 240 MeV except for 27.0 and 34.0 MeV in the backward-angle area,where the calculations are smaller than the experimental data (for the discussion, see Fig. 2). In this figure, the elastic-scattering angular distributions at 318.0 and 350.0 MeV are also predicted and compared with the experimental data [66,67]. In principle the present model is not appropriate for extending predictions beyond 250 MeV. Here, we only perform a tentative calculation for the lighter target ^{28}Si. The curve shapes of the calculations are similar to that of the experimental data although there are some discrepancies between them.

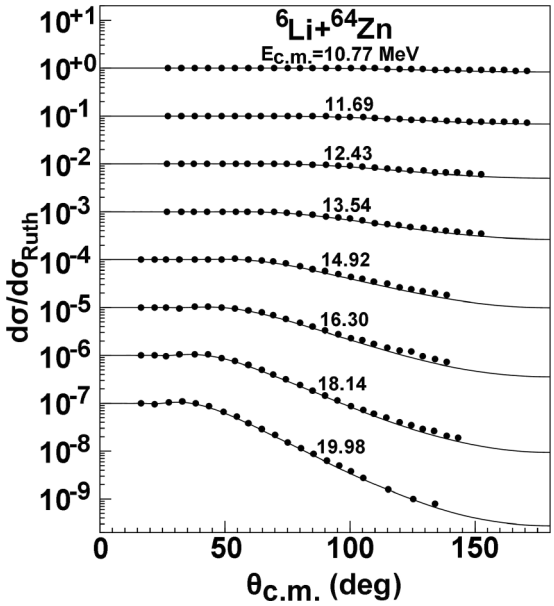

FIG. 13. The same as Fig. 10 but for ^{64}Zn [35].

The elastic-scattering angular distributions are calculated using the global ^{6}Li OMP for ^{54}Fe at incident energies of 38.0, 44.0, and 50.0 MeV. By comparing with the experimental data [26], it can be found that the results yield a good fit to the data. For ^{59}Co, good agreement with the data [27] is also obtained at incident energies of 12.0, 18.0, 26.0, and 30.0 MeV. The similar

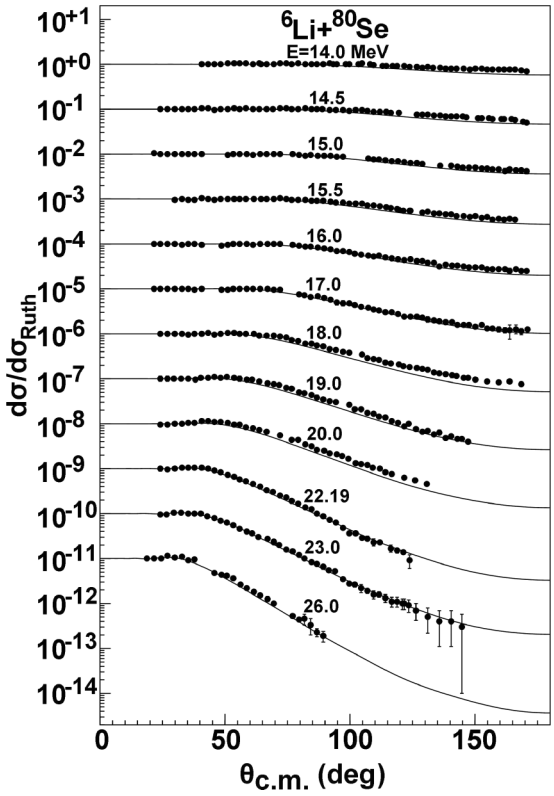

FIG. 14. The same as Fig. 10 but for ^{80}Se [36].

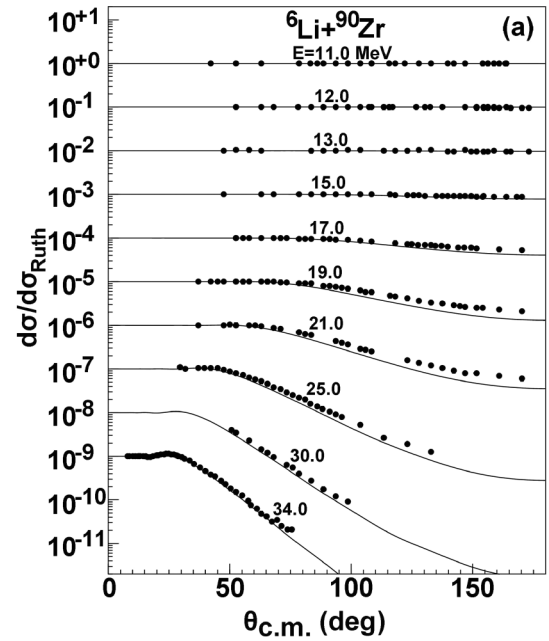

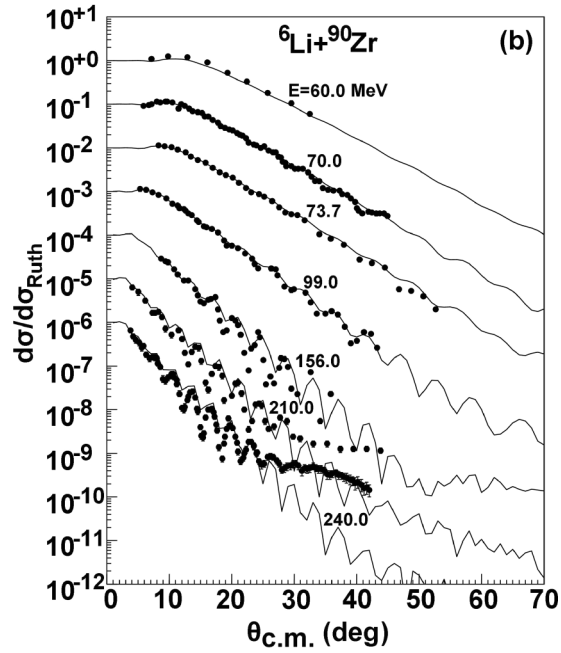

FIG. 15. The same as Fig. 10 but for ^{90}Zr [9,18,21,25,30,37–40].

analysis is applied to the elastic angular distributions of ^{58}Ni below 240 MeV. The results in the Rutherford ratio are further compared with the experimental data [18,23,25,28–32,68]. The calculations are slightly smaller than the experimental data [68] above 100°. However, good agreements with the experimental data [28] are obtained below 14.04 MeV as is shown in Fig. 12(a). For the other incident energies, the close agreements between the calculations and the data are achieved except for 210.0 and 240.0 MeV where the calculations are slightly smaller than the experimental data [25,32] above about 25°. The results are shown in Fig. 12(b).

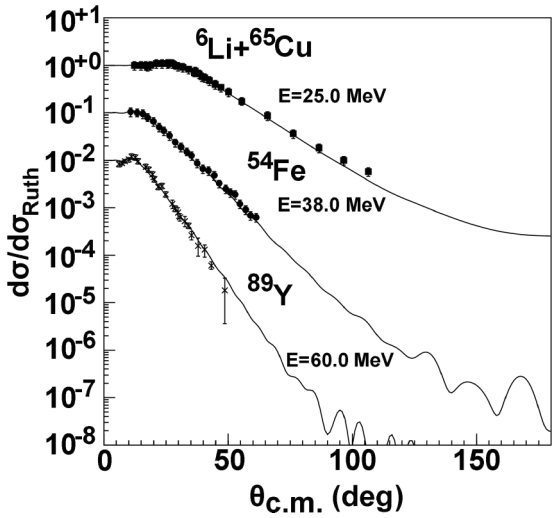

FIG. 16. The same as Fig. 10 but for ^{65}Cu, ^{54}Fe, and ^{89}Y [26,34,37].

The elastic-scattering angular distributions for ^{64}Zn are calculated at incident energies from 10.77 to 19.98 MeV in the center-of-mass system. Comparisons between our calculations and the experimental data [35] show that excellent agreement is obtained. The results are plotted in Fig. 13. The elastic-scattering angular distributions for relatively medium-mass target ^{80}Se at incident energies from 14.0 to 26.0 MeV are also calculated using the global OMP, which is displayed in Fig. 14. The calculations also provide good fits to the experimental data [36].

The calculations of elastic-scattering angular distributions for ^{90}Zr are compared with the experimental data [9,18,21,25,30,37–40] in a wide range of incident energies, which is shown in Fig. 15. In the whole energy range, good agreement is also observed between the theoretical calculations and the experimental value except for 210.0 and 240.0 MeV above 25°.

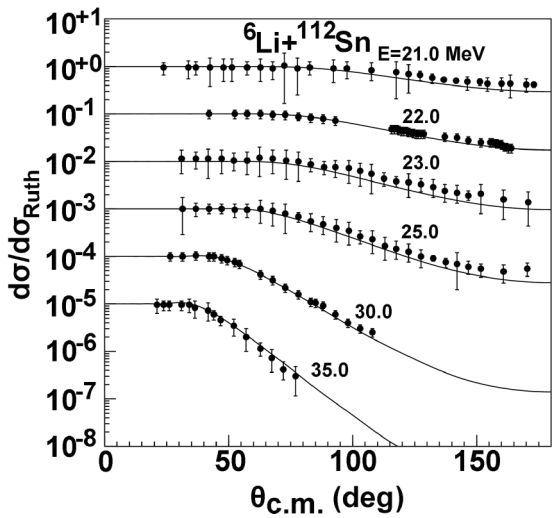

FIG. 17. The same as Fig. 10 but for ^{112}Sn [41,42].

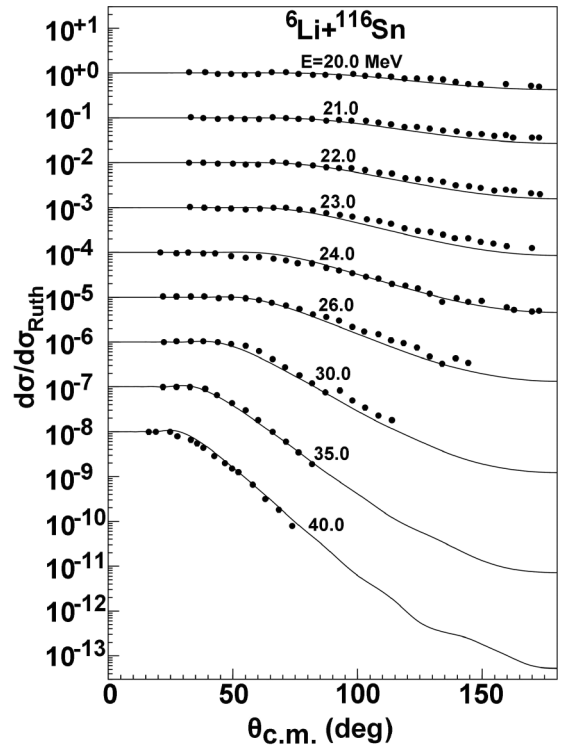

FIG. 18. The same as Fig. 10 but for ^{116}Sn [43].

Moreover, the elastic-scattering angular distributions for some relatively medium-mass targets are measured at single incident energy. The elastic-scattering angular distributions for ^{65}Cu, ^{54}Fe, and ^{89}Y are also calculated and compared with the corresponding experimental data [26,34,37] at different incident energies, which is shown in Fig. 16. One can see that the results calculated using the ^{6}Li global phenomenological OMP are also consistent with the experimental data.

The elastic-scattering angular distributions for the tin isotopes chain ^{112,116,120}Sn are calculated and compared with the existing experimental data [31,41–43,45,46]. For ^{112,120}Sn, the calculations can well reproduce the existing experimental data.

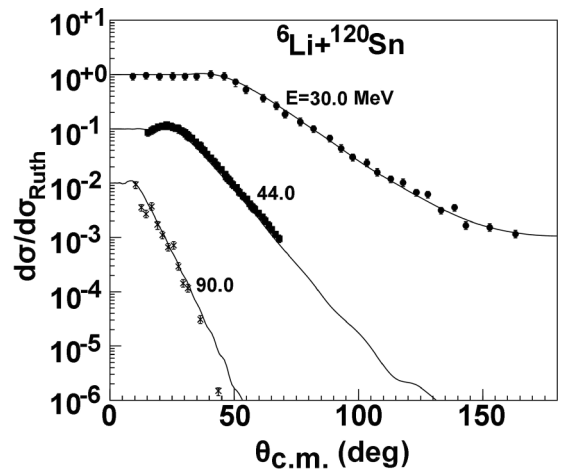

FIG. 19. The same as Fig. 10 but for ^{120}Sn [31,45,46].

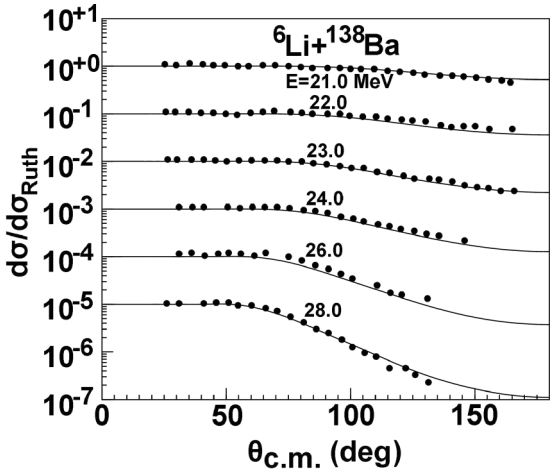

FIG. 20. The same as Fig. 10 but for ^{138}Ba [47].

In the case of ^{116}Sn, it is found that there are some discrepancies between the calculations and the experimental data [41]. But the calculations reproduce the newest elastic-scattering data [43] well over the entire energy range of measurement. These results are shown in Figs. 17–19.

The elastic-scattering angular distributions for ^{138}Ba and ^{144}Sm are also calculated using the ^{6}Li global phenomenological OMP. The calculations along with the measured data [47,48] are displayed in Figs. 20 and 21. From these figures, one can see that this potential can reproduce the

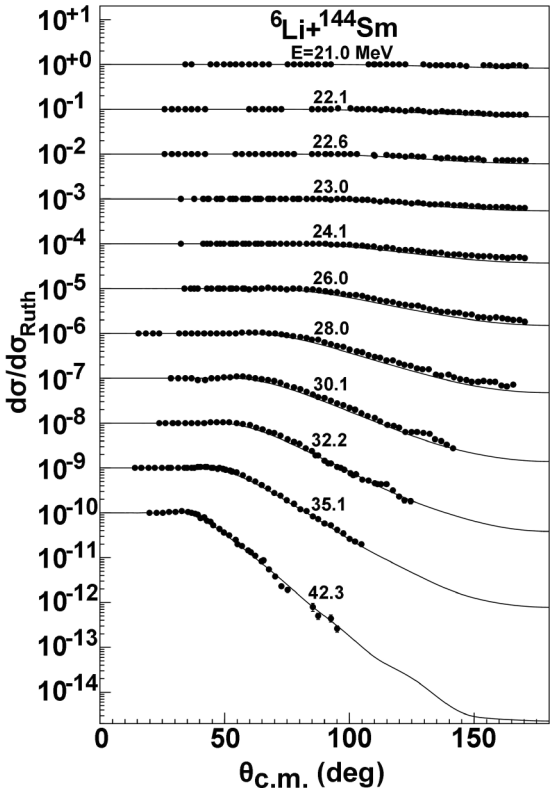

FIG. 21. The same as Fig. 10 but for ^{144}Sm [48].

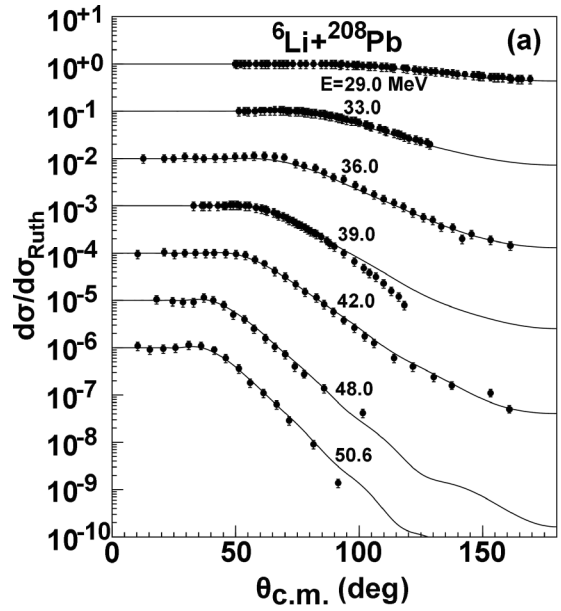

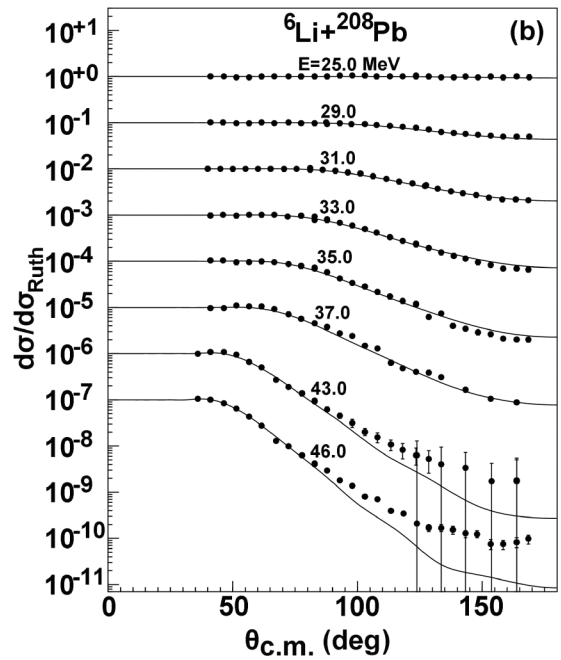

FIG. 22. The same as Fig. 10 but for ^{208}Pb [23,49–51].

elastic-scattering angular distributions data well for ^{138}Ba and ^{144}Sm over the entire energy range of measurement.

For ^{208}Pb, the elastic-scattering angular distributions are compared with the data from the different experiments, which is shown in Fig. 22. From Fig. 22(a), it can be observed that the calculated results reproduce the experimental data [23,50,51] well except for 39.0 MeV where the calculations overestimate the experimental data [50] above 100°. Figure 22(b) shows the comparisons between the calculations and the experimental data [49] below 46.0 MeV. It can be seen that the calculations are in good agreement with the data except for 46.0 MeV above about 100° where the calculations underestimate the experimental data. For incident energies above 70.0 MeV, as

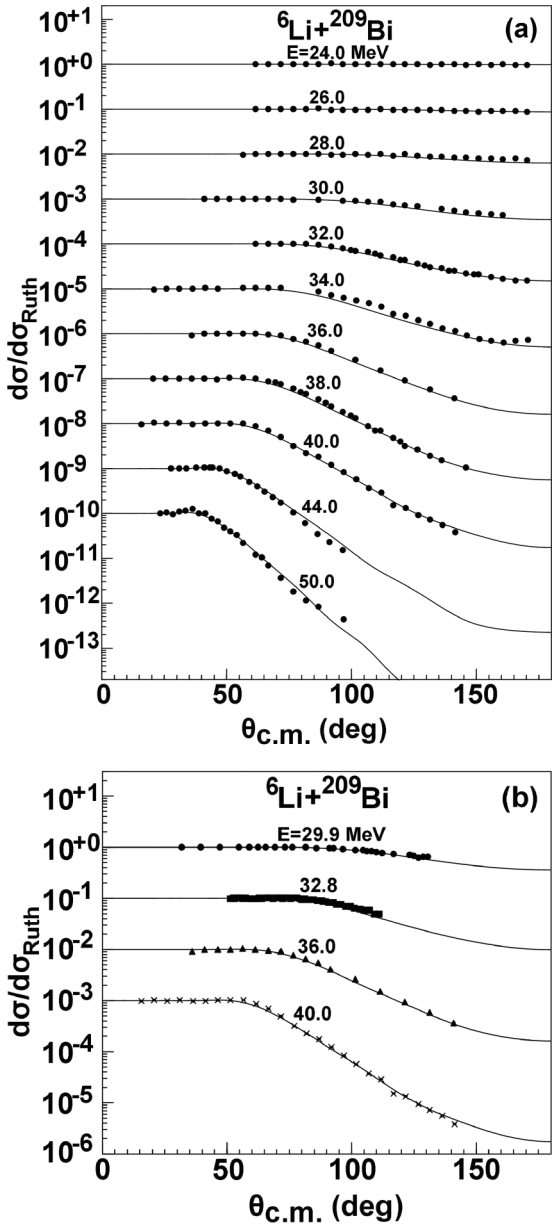

FIG. 23. The same as Fig. 10 but for ^{209}Bi [53–55].

mentioned earlier and shown in Fig. 4, the results calculated using the global phenomenological OMP overestimate the experimental data [30] for ^{208}Pb in the backward-angle area.

A similar analysis is also applied to the elastic-scattering angular distributions for the nearby nucleus ^{209}Bi. The calculations of elastic-scattering angular distributions are also compared with the data measured from different experiments. The results are shown in Fig. 23. From Fig. 23(a) one can see that the calculations well reproduce the data [53] from 24.0 to 50.0 MeV. In addition, the calculations give excellently well descriptions of the elastic angular distributions from the other experiments [54,55], which are shown in Fig. 23(b). Up to now, there have been no experimental data above 70.0 MeV.

To further improve fits to the data for ^{208}Pb, the radius parameters of the real part for the global phenomenological

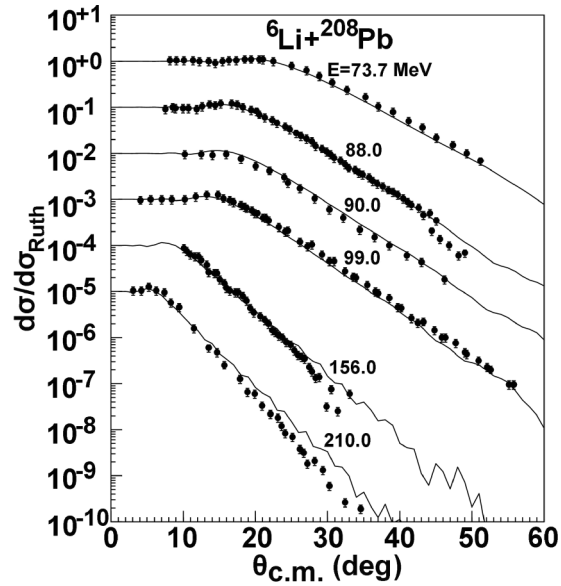

FIG. 24. The same as Fig. 22 but for above 70 MeV [9,18,21,30,31,52].

OMP is added by 0.1. Figure 24 shows the elastic-scattering angular distributions calculated using the new parameters of the global OMP above 70 MeV From this figure, it can be clearly seen that the calculations give a better description of the experimental data [9,18,21,30,31,52] except for 210 MeV above 20°.

In order to investigate the reliability of the ^{6}Li global OMP, the elastic-scattering angular distributions for some targets are also measured at the same incident angles with different incident energies. The comparisons between the optical model calculations and the corresponding experimental data are performed for different targets. Figure 25 displays the elastic-scattering angular distributions for ^{27}Al at incident angles 140.0°, 165.0°, and 170.0°. It can be seen that the ^{6}Li OMP gives a good description of the experimental data [69,70] in the error range. The elastic-scattering angular distributions

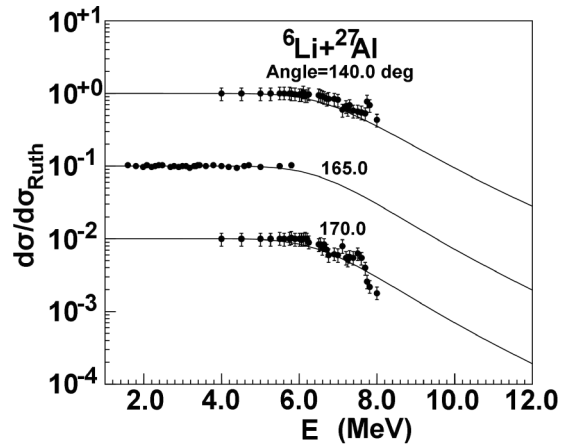

FIG. 25. Calculated elastic-scattering angular distributions in the Rutherford ratio at the same incident angle compared with the experimental data [69,70] for ^{27}Al.

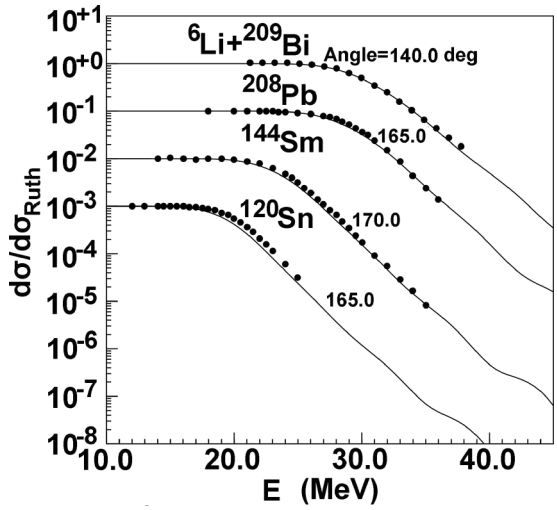

FIG. 26. The same as Fig. 25 but for ^{120}Sn, ^{144}Sm, ^{208}Pb, and ^{209}Li [71–73].

for ^{48}Ti are also compared with the experimental data [70] at 140° and 170°. Good agreement is also obtained in the error range.

The elastic-scattering angular distributions for ^{120}Sn, ^{144}Sm, ^{208}Pb, and ^{209}Bi are also compared with the experimental data [71–73] at incident angles of 140.0°, 165.0°, and 170.0° as shown in Fig. 26. The calculations are in reasonable agreement with the experimental data.

Moreover, the reaction cross section is also an important observable of the optical model. It has long been of interest since it is intended to test nuclear models, get information about projectile matter distributions, and give clues to their structures. For instance, accurate elastic-scattering measurements can determine the optical model potential parameters for a system, which in turn allow reaction cross sections to be deduced. On the other hand, the reaction cross-sectional values can serve as important constraints in phenomenological optical model analyses [74]. Thus, the reaction cross sections are also calculated using our global OMP for different targets, and they are further compared with the existing data. The reaction cross sections for ^{27}Al calculated using the obtained ^{6}Li global OMP are presented in Fig. 27. There is only an experimental dot [57] above 200 MeV. The reaction cross-sectional data at four energies close to the Coulomb barrier were extracted from the optical model fits [56]. The calculations are consistent with these data.

Figure 28 shows the reaction cross sections calculated using the global OMP for ^{63,65}Cu and ^{64}Zn. There are no experimental data of reaction cross sections for ^{63,65}Cu. We compare the results with the experimental data [58] of the $^{nat.}$Cu target. Reasonable agreements are achieved below 250 MeV for ^{63,65}Cu. There are also some data above 250 MeV from the same experiment. The calculations are compared with these data, and good agreement is obtained. For ^{64}Zn, the data are derived from the experimental elastic-scattering angular distributions for the ^{6}Li + ^{64}Zn systems [35,59] at energies from below to above the Coulomb barrier. From the figure, it

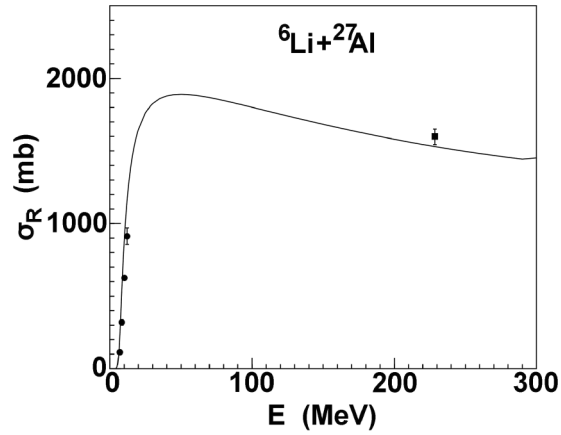

FIG. 27. Comparison between the optical model calculation and the experimental data [56,57] of ^{6}Li reaction cross sections for ^{27}Al.

can be seen the calculations are also in excellent agreement with these data [35,59].

The reaction cross sections for ^{112,116}Sn are calculated using the global OMP. There are only the reaction cross-sectional data derived from the experimental elastic-scattering data for the ^{6}Li + ^{112,116}Sn systems [41] at energies near the Coulomb barrier. The calculations are compared with these data, which are shown in Fig. 29. One can see that the reaction cross

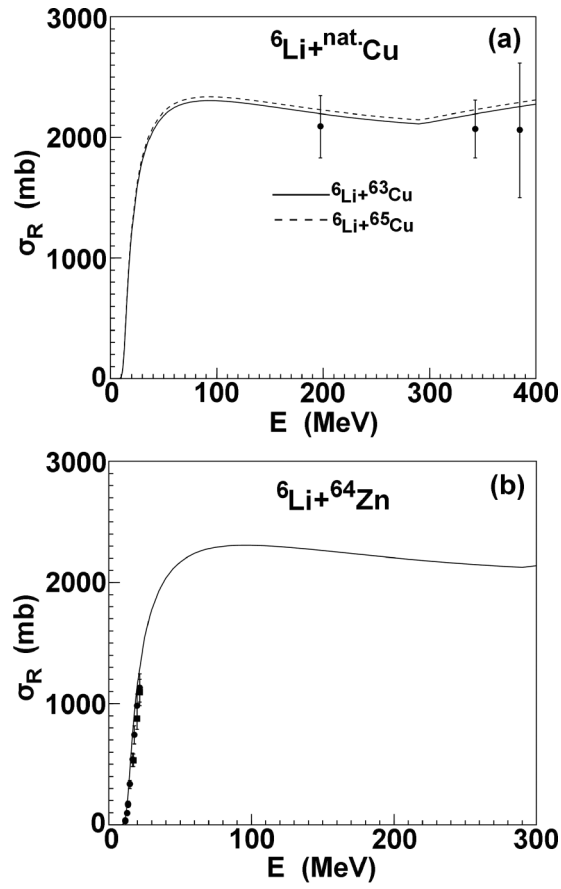

FIG. 28. The same as Fig. 27 but for ^{63,65}Cu and ^{64}Zn [35,58,59].

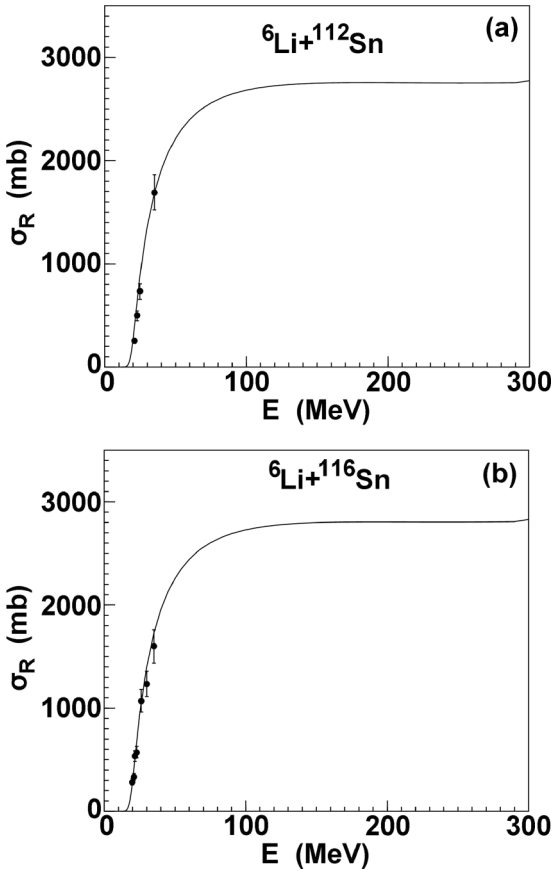

FIG. 29. The same as Fig. 27 but for ^{112,116}Sn [41].

sections are in satisfactory agreement with the data extracted from the measured elastic-scattering angular distributions for both of them.

Furthermore, the reaction cross sections for ^{138}Ba are compared with the corresponding data which are extracted from the elastic-scattering angular distributions for the ^{6}Li + ^{138}Ba systems at sub- and near-barrier energies [47]. Good agreement is achieved between them, which is shown in Fig. 30.

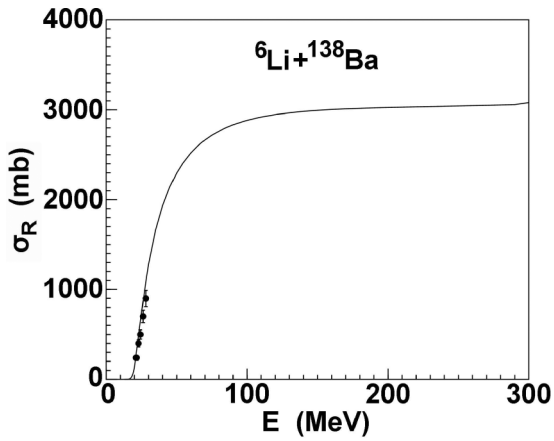

FIG. 30. The same as Fig. 27 but for ^{138}Ba [47].

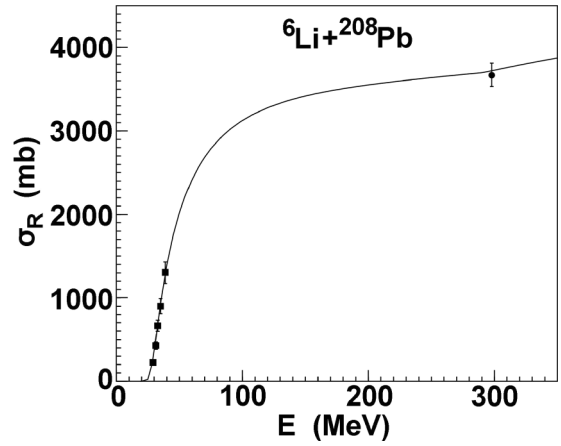

FIG. 31. The same as Fig. 27 but for ^{208}Pb [50,60].

The reaction cross sections for ^{208}Pb are also calculated using the ^{6}Li global OMP. The data of the reaction cross sections [50] are derived in terms of the optical model by analyzing the elastic-scattering data at several energies near the Coulomb barrier. The agreement with the data is rather good. In addition, the reaction cross sections on $^{nat.}$Pb were measured at 298.0 meV [60]. The calculations are also compared with the experimental data and agree well with the data. These results are shown in Fig. 31. In addition, from the above results of the reaction cross sections, it is observed that there is a common tendency that the reaction cross sections for heavy nuclei increase with increasing incident energy from Coulomb barrier up to 200 MeV. However, they increase first and then slightly decrease with increasing incident energy for light targets.

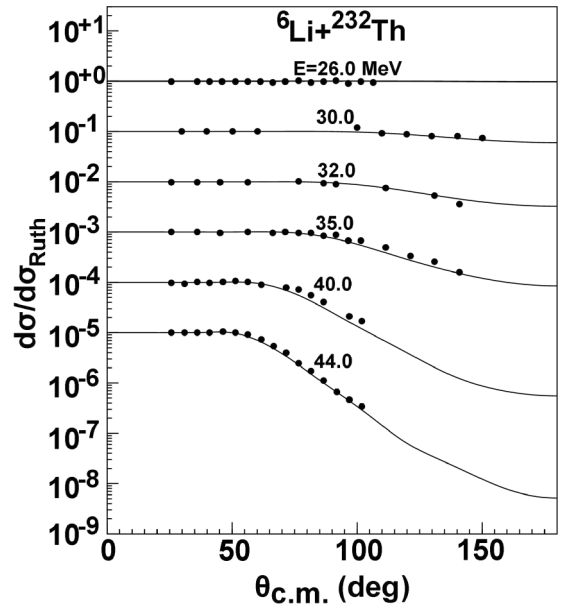

FIG. 32. Comparison between the optical model prediction and the experimental data [75] of ^{6}Li elastic-scattering angular distributions for ^{232}Th.

Moreover, the calculations of elastic-scattering angular distributions for those targets in the mass ranges of $7 \leqslant A \leqslant 24$ and $209 < A \leqslant 239$ are further predicted at different incident energies. These targets are some lighter and deformed nuclei. From the comparison with the experimental data, it is found that the predictions are also in reasonable agreement with experimental data for actinide nuclei. The results of elastic-scattering angular distributions for some light targets slightly underestimate the experimental data in the backward-angle area. But the curve shapes of the calculated elastic-scattering angular distributions are similar with the corresponding experimental data. Figure 32 gives the comparisons with the experimental data [75] for ^{232}Th from 26.0 to 44.0 MeV. Good agreement is observed between them.

IV. SUMMARY AND CONCLUSIONS

Within the framework of the optical model, a new set of ^{6}Li global phenomenological energy-dependent optical potential parameters based on the form of the Woods-Saxon potential has been found. The potential simultaneously fits the experimental elastic-scattering angular distributions and reaction cross sections for the mass range of target nuclei from 24 to 209 at incident energies below 250 MeV. By comparing with the experimental data, the global OMP of the ^{6}Li projectile which is obtained has been shown to provide a good description of ^{6}Li elastic scattering below 200 MeV. There are some divergencies between the calculations and the experimental data for some targets at incident energies of 210.0 and 240.0 MeV. The reason may be that the breakup effects of the ^{6}Li projectile are not considered in the calculations. To thoroughly investigate the breakup effects of the projectile ^{6}Li, the CDCC method will be applied to analyses of the scattering and the breakup of the ^{6}Li projectile in future work. On the other hand, in order to investigate the reliability of the global OMP, the isotope chains for some targets are predicted at different incident energies. Moreover, the predictions are also performed for the mass number of target nuclei $A < 24$ and the actinide nuclei. Comparisons with the experimental data show that the predictions are also reasonable for them. The performed calculations reveal that the obtained ^{6}Li global OMP will be significant to investigators performing systematic studies for nuclear model calculations and experimental analysis involving weakly bound nucleus ^{6}Li scattering especially for the breakup or transfer reactions.

ACKNOWLEDGMENTS

This work was supported by the China National Natural Science Foundation under Grants No. 11405099 and No. 11575291. This work is also a part of the IAEA Coordinated Research Projects on the Recommended Input Parameter Library for Fission Cross Section Calculations under Contract No. 20464.

[1] P. E. Hodgson, *The Optical Model of Elastic Scattering* (Clarendon, Oxford, 1963).
[2] A. J. Koning and J. P. Delaroche, Nucl. Phys. A **713**, 231 (2003).
[3] A. Pakou, N. Alamanos, A. Lagoyannisa, A. Gillibert, E. C. Pollacco, P. A. Assimakopoulos, G. Doukelis, K. G. Ioannides, D. Karadimos, D. Karamanis *et al.*, Phys. Lett. B **556**, 21 (2003).
[4] J. Thompson and M. A. Nagarajan, Phys. Lett. B **106**, 163 (1981).
[5] Y. Sakuragi, M. Yahiro, and M. Kamimura, Prog. Theor. Phys. **68**, 322 (1982).
[6] A. Gómez Camacho, P. R. S. Gomes, and J. Lubian, Phys. Rev. C **82**, 067601 (2010).
[7] P. Schwandt, W. W. Jacobs, M. D. Kaitchuck, P. P. Singh, W. D. Ploughe, F. D. Becchetti, and J. Janecke, Phys. Rev. C **24**, 1522 (1981).
[8] B. Canbula, D. Canbula, and H. Babacan, Phys. Rev. C **91**, 044615 (2015).
[9] J. Cook, Nucl. Phys. A **388**, 153 (1982).
[10] Q. B. Shen, Nucl. Sci. Eng. **141**, 78 (2002).
[11] B. Alder, S. Fernbach, and M. Rotenberg, *Methods in Computational Physics* (Academic Press, New York, 1966).
[12] X. Chen, Y.-W. Lui, H. L. Clark, Y. Tokimoto, and D. H. Youngblood, Phys. Rev. C **80**, 014312 (2009).
[13] G. Ciangaru, R. L. McGrath, and F. E. Cecil, Nucl. Phys. A **380**, 147 (1982).
[14] J. M. Figueira, J. O. Fernandez Niello, D. Abriola, A. Arazi, O. A. Capurro, E. De Barbara, G. V. Marti, D. Martinez Heimann *et al.*, Phys. Rev. C **75**, 017602 (2007).
[15] M. Sinha, S. Roy, P. Basu, H. Majumdar, S. Santra, V. V. Parkar, K. S. Golda, and S. Kailas, EPJ Web Conf. **17**, 03004 (2011).
[16] M. Hugi, J. Lang, R. Mueller, E. Ungricht, K. Bodek, L. Jarczyk, B. Kamys, A. Magiera, A. Strzalkowski, and G. Willim, Nucl. Phys. A **368**, 173 (1981).
[17] M. F. Vineyard, J. Cook, and K. W. Kemper, Nucl. Phys. A **405**, 429 (1983).
[18] D. P. Stanley, F. Petrovich, and P. Schwandt, Phys. Rev. C **22**, 1357 (1980).
[19] R. M. de Vries, D. A. Goldberg, J. W. Watson, M. S. Zisman, and J. G. Cramer, Phys. Rev. Lett. **39**, 450 (1977).
[20] P. Schwandt, S. Kailas, W. W. Jacobs, M. D. Kaitchuck, W. Ploughe, and P. P. Singh, Phys. Rev. C **21**, 1656 (1980).
[21] A. Nadasen, M. McMaster, M. Fingal, J. Tavormina, P. Schwandt, J. S. Winfield, M. F. Mohar, F. D. Becchetti, J. W. Janecke, and R. E. Warner, Phys. Rev. C **39**, 536 (1989).
[22] J. Szymakowski, K. W. Kemper, and A. D. Frawley, Nucl. Phys. A **355**, 221 (1981).
[23] L. T. Chua, F. D. Becchetti, J. Janecke, and F. L. Milder, Nucl. Phys. A **273**, 243 (1976).
[24] Z. Majka, H. J. Gils, and H. Rebel, Z. Phys. A: At. Nucl. **288**, 139 (1978).
[25] Krishichayan, X. Chen, Y.-W. Lui, J. Button, and D. H. Youngblood, Phys. Rev. C **81**, 044612 (2010).
[26] K. W. Kemper, A. F. Zeller, T. R. Ophel, D. F. Hebbard, A. Johnston, and D. C. Weisser, Nucl. Phys. A **320**, 413 (1979).
[27] F. A. Souza, L. A. S. Leal, N. Carlin, M. G. Munhoz, R. Liguori Neto, M. M. de Moura, A. A. P. Suaide, E. M. Szanto, A.

Szanto de Toledo, and J. Takahashi, Phys. Rev. C **75**, 044601 (2007).
[28] E. F. Aguilera, E. Martinez-Quiroz, D. Lizcano, A. Gomez-Camacho, J. J. Kolata, L. O. Lamm, V. Guimaraes, R. Lichtenthaler, O. Camargo, F. D. Becchetti *et al.*, Phys. Rev. C **79**, 021601 (2009).
[29] K. D. Veal, C. R. Brune, W. H. Geist, H. J. Karwowski, E. J. Ludwig, E. E. Bartosz, P. D. Cathers, T. L. Drummer, K. W. Kemper, A. M. Eiro *et al.*, Phys. Rev. C **60**, 064003 (1999).
[30] R. Huffman, A. Galonsky, R. Markham, and C. Williamson, Phys. Rev. C **22**, 1522 (1980).
[31] Y. A. Glukhov, A. S. Demyanova, V. I. Manko, B. G. Novatsky, A. A. Ogloblin, S. B. Sakuta, D. N. Stepanov, and V. I. Chuev, Institut Atomnoy Energii, Kurchatov Report No. IAE-2989 (unpublished).
[32] A. Nadasen, M. McMaster, G. Gunderson, A. Judd, S. Villanueva, P. Schwandt, J. S. Winfield, J. van der Plicht, R. E. Warner, F. D. Becchetti *et al.*, Phys. Rev. C **37**, 132 (1988).
[33] Krishichayan, X. Chen, Y. W. Lui, Y. Tokimoto, J. Button, and D. H. Youngblood, Phys. Rev. C **81**, 014603 (2010).
[34] A. Shrivastava, A. Navin, N. Keeley, K. Mahata, K. Ramachandran, V. Nanal, V. V. Parkar, A. Chatterjee, and S. Kailas, Phys. Lett. B **633**, 463 (2006).
[35] M. Zadro, P. Figuera, A. Di Pietro, F. Amorini, M. Fisichella, O. Goryunov, M. Lattuada, C. Maiolino, A. Musumarra, V. Ostashko *et al.*, Phys. Rev. C **80**, 064610 (2009).
[36] L. Fimiani, J. M. Figueira, G. V. Marti, J. E. Testoni, A. J. Pacheco, W. H. Z. Ca Rdenas, A. Arazi, O. A. Capurro, M. A. Cardona, P. Carnelli *et al.*, Phys. Rev. C **86**, 044607 (2012).
[37] R. Wadsworth, M. D. Cohler, M. J. Smithson, D. L. Watson, F. Jundt, L. Kraus, I. Linck, and J. C. Sens, J. Phys. G: Nucl. Part. Phys. **9**, 1237 (1983).
[38] H. Kumawat, V. Jha, B. J. Roy, V. V. Parkar, S. Santra, V. Kumar, D. Dutta, P. Shukla, L. M. Pant, A. K. Mohanty *et al.*, Phys. Rev. C **78**, 044617 (2008).
[39] R. J. Puigh and K. W. Kemper, Nucl. Phys. A **313**, 363 (1979).
[40] D. J. Horen, R. L. Auble, J. Gomez del Campo, G. R. Satchler, R. L. Varner, J. R. Beene, B. Lund, V. R. Brown, P. L. Anthony, and V. A. Madsen, Phys. Rev. C **47**, 629 (1993).
[41] N. N. Deshmukh, S. Mukherjee, B. K. Nayak, D. C. Biswas, S. Santra, E. T. Mirgule, S. Appannababu, D. Patel, A. Saxena, R. K. Choudhury *et al.*, Eur. Phys. J. A **47**, 118 (2011).
[42] D. Chattopadhyay, S. Santra, A. Pal, A. Kundu, K. Ramachandran, R. Tripathi, D. Sarkar, S. Sodaye, B. K. Nayak, A. Saxena *et al.*, Phys. Rev. C **94**, 061602 (2016).
[43] D. Patel, S. Mukherjee, N. Deshmukh, J. Lubian, J.-S. Wang, T. Correa, B. K. Nayak, Y.-Y. Yang, W.-H. Ma, D. C. Biswas *et al.*, Chin. Phys. C **41**, 104001 (2017).
[44] A. F. Zeller, K. W. Kamper, T. R. Ophel, D. C. Weisser, D. F. Hebbard, A. Johnston, and G. T. Hickey, Nucl. Phys. A **309**, 255 (1978).
[45] V. V. Davydov, B. G. Novashkii, A. A. Ogloblin, S. B. Sakuta, D. N. Stepanov, and V. I. Chuev, Bull. Russian Acad. Sci. **35**, 2176 (1972).
[46] K. Becker, K. Blatt, H. J. Jansch, W. Korsch, H. Leucker, W. Luck, H. Reich, H.-G. Volk, D. Fick, and K. Rusek, Nucl. Phys. A **535**, 189 (1991).
[47] A. M. M. Maciel, P. R. S. Gomes, J. Lubian, R. M. Anjos, R. Cabezas, G. M. Santos, C. Muri, S. B. Moraes, R. Liguori Neto, N. Added *et al.*, Phys. Rev. C **59**, 2103 (1999).
[48] J. M. Figueira, J. O. Fernandez Niello, A. Arazi, O. A. Capurro, P. Carnelli, L. Fimiani, G. V. Marti, D. Martinez Heimann, A. E. Negri *et al.*, Phys. Rev. C **81**, 024613 (2010).
[49] C.-L. Zhang, H.-Q. Zhang, C.-J. Lin, M. Ruan, Z.-H. Liu, F. Yang, X.-K. Wu, P. Zhou, G.-P. An, and H.-M. Jia, Chin. Phys. Lett. **23**, 1146 (2006).
[50] N. Keeley, S. J. Bennett, N. M. Clarke, B. R. Fulton, G. Tungate, P. V. Drumm, M. A. Nagarajan, and J. S. Lilley, Nucl. Phys. A **571**, 326 (1994).
[51] H. Gemmeke, B. Deluigi, L. Lassen, and D. Scholz, Z. Phys. A: At. Nucl. **286**, 73 (1978).
[52] C. B. Fulmer, G. R. Satchler, E. E. Gross, F. E. Bertrand, C. D. Goodman, D. C. Hensley, J. R. Wu, N. M. Clarke, and M. F. Sleeden, Nucl. Phys. A **356**, 235 (1981).
[53] S. Santra, S. Kailas, K. Ramachandran, V. V. Parkar, V. Jha, B. J. Roy, and P. Shukla, Phys. Rev. C **83**, 034616 (2011).
[54] N. Keeley, J. M. Cook, K. W. Kemper, B. T. Roeder, W. D. Weintraub, F. Marechal, and K. Rusek, Phys. Rev. C **68**, 054601 (2003).
[55] S. Santra, V. V. Parkar, K. Ramachandran, U. K. Pal, A. Shrivastava, B. J. Roy, B. K. Nayak, A. Chatterjee, R. K. Choudhury, and S. Kailas, Phys. Lett. B **677**, 139 (2009).
[56] E. A. Benjamim, A. Lepine-Szily, D. R. Mendes, Jr., R. Lichtenthaler, V. Guimaraes, P. R. S. Gomes, L. C. Chamon, M. S. Hussein, A. M. Moro, A. Arazi *et al.*, Phys. Lett. B **647**, 30 (2007).
[57] M. Fukuda, M. Mihara, T. Fukao, S. Fukuda, M. Ishihara, S. Ito, T. Kobayashi, K. Matsuta, T. Minamisono, S. Momota *et al.*, Nucl. Phys. A **656**, 209 (1999).
[58] M. G. Saint-Laurent, R. Anne, D. Bazin, D. Guillemaud-Mueller, U. Jahnke, J. G. Ming, A. C. Mueller, J. F. Bruandet, F. Glasser, S. Kox *et al.*, Z. Phys. A: At. Nucl. **332**, 457 (1989).
[59] P. R. S. Gomes, M. D. Rodriguez, G. V. Marti, I. Padron, L. C. Chamon, J. O. Fernandez Niello, O. A. Capurro, A. J. Pacheco, J. E. Testoni, A. Arazi *et al.*, Phys. Rev. C **71**, 034608 (2005).
[60] R. E. Warner, M. H. McKinnon, N. C. Shaner, F. D. Becchetti, A. Nadasen, D. A. Roberts, J. A. Brown, A. Galonsky, J. J. Kolata, R. M. Ronningen *et al.*, Phys. Rev. C **62**, 024608 (2000).
[61] V. V. Parkar, S. K. Pandit, A. Shrivastava, R. Palit, K. Mahata, V. Jha, K. Ramachandran, S. Gupta, S. Santra, S. K. Sharma *et al.*, Phys. Rev. C **98**, 014601 (2018).
[62] Y. Sakuragi, M. Yahiro, and M. Kamimura, Prog. Theor. Phys. Suppl. **89**, 136 (1986).
[63] Y. Sakuragi, Phys. Rev. C **35**, 2161 (1987).
[64] Y. Sakuragi, M. Ito, Y. Hirabayashi, and C. Samanta, Prog. Theor. Phys. **98**, 521 (1997).
[65] M. D. L. Barbosa, T. Borello-Lewin, L. B. Horodynski-Matsushigue, J. L. M. Duarte, C. L. Rodrigues, M. R. D. Rodrigues, and G. M. Ukita, Phys. Rev. C **71**, 024303 (2005).
[66] A. Nadasen, T. Stevens, J. Farhat, J. Brusoe, P. Schwandt, J. S. Winfield, G. Yoo, N. Anantaraman, F. D. Becchetti, J. Brown *et al.*, Phys. Rev. C **47**, 674 (1993).
[67] A. Nadasen, J. Brusoe, J. Farhat, T. Stevens, J. Williams, L. Nieman, J. S. Winfield, R. E. Warner, J. W. Jaenecke, T. Annakkage *et al.*, Phys. Rev. C **52**, 1894 (1995).
[68] M. Biswas, S. Roy, M. Sinha, M. K. Pradhan, A. Mukherjee, P. Basu, H. Majumdar, K. Ramachandran, and A. Shrivastava, Nucl. Phys. A **802**, 67 (2008).
[69] M. Mayer, B. Diaz-Herrera, and M. Schneider, Nucl. Instrum. Methods Phys. Res., Sect. B **207**, 263 (2003).

[70] A. Nurmela, E. Rauhala, and J. Raisanen, Nucl. Instrum. Methods Phys. Res., Sect. B **155**, 211 (1999).

[71] K. Zerva, A. Pakou, N. Patronis, P. Figuera, A. Musumarra, A. Di Pietro, M. Fisichella, T. Glodariu, M. La Commara, M. Lattuada *et al.*, Eur. Phys. J. A **48**, 102 (2012).

[72] D. S. Monteiro, O. A. Capurro, A. Arazi, J. O. Fernandez Niello, J. M. Figueira, G. V. Marti, D. Martinez Heimann, A. E. Negri, A. J. Pacheco, V. Guimaraes *et al.*, Phys. Rev. C **79**, 014601 (2009).

[73] D. Patel, S. Mukherjee, B. K. Nayak, S. V. Suryanarayana, D. C. Biswas, E. T. Mirgule, Y. K. Gupta, L. S. Danu, B. V. John, and A. Saxena, Phys. Rev. C **89**, 064614 (2014).

[74] R. E. Warner, R. A. Patty, P. M. Voyles, A. Nadasen, F. D. Becchetti, J. A. Brown, H. Esbensen, A. Galonsky, J. J. Kolata, J. Kruse *et al.*, Phys. Rev. C **54**, 1700 (1996).

[75] S. Dubey, S. Mukherjee, D. C. Biswas, B. K. Nayak, D. Patel, G. K. Prajapati, Y. K. Gupta, B. N. Joshi, L. S. Danu, S. Mukhopadhyay *et al.*, Phys. Rev. C **89**, 014610 (2014).